ADVANCED MATERIALS
www.advmat.de

Ultrahigh-Sensitivity Sandwiched Plasmon Ruler for Label-Free Clinical Diagnosis

Jingjie Nan, Shoujun Zhu, Shunsheng Ye, Weihong Sun, Ying Yue, Xiaoduo Tang, Jingwei Shi, Xuesong Xu, Junhu Zhang,* and Bai Yang*

Optical biosensors, especially those based on plasmonic structures, have emerged recently as a potential tool for disease diagnostics. Plasmonic biosensors have demonstrated impressive benefits for the label-free detection of trace biomarkers in human serum. However, widespread applications of these technologies are hindered because of their insufficient sensitivity, their relatively complex chemical immobilization processes, and the use of prism couplers. Accordingly, a sandwiched plasmon ruler (SW-PR) based on a Au nanohole array with ultrahigh sensitivity arising from the plasmonic coupling effect is developed. Highly confined surface charges caused by Bloch wave surface plasmon polarizations substantially increase the coupling efficiency. This platform exhibits thickness sensitivity as high as 61 nm nm^{-1} and can detect at least 200 000-fold lower analyte concentrations than a nanowell sensing platform with the same wavelength shift. Additionally, the sandwiched plasmonic biosensor allows precise and label-free testing of clinical biomarkers, namely C-reactive protein and procalcitonin, in patient serum samples without requiring a sophisticated prism coupler, extra antibodies, or a chemical immobilization technique. This study yields new insight into the structural design of plasmon rulers and will open exciting avenues for disease diagnosis and therapy follow-up at the point-of-care.

Surface plasmons are known as powerful tools for the rapid label-free detection of biomolecular interactions in the field of clinical diagnosis.[1–4] Coherent oscillations of conduction electrons on a metal surface are extremely sensitive to refractive index (RI) changes of the surrounding medium, endowing plasmonic biosensors with the ability to monitor binding events in real time.[5–9] Recently, many of the potential means of improving detection sensitivity have arisen from the development of new plasmonic structures. There are also significant efforts aimed at miniaturizing and integrating the sensing platform, making plasmonic biosensors a great candidate for point-of-care (POC) diagnosis.[10,11]

A standard plasmonic biosensor relies on either propagating surface plasmon polaritons (SPPs) excited on a continuous metal surface or localized surface plasmon resonance (LSPR) excited within a metal nanoparticle or nanostructure.[12] SPP-based sensors are thought to have high refractive index sensitivity (RIS) and long electromagnetic decay lengths. However, SPP sensors employ a Kretschmann configuration associated with bulky instruments and a high detection cost to effectively excite SPP signals, which consequently makes SPP-based sensors inadequate for POC diagnosis.[13] In striking contrast, LSPR confines collective oscillations of free electrons to the nanoscale, affording high-efficiency signal readout without using a prism coupler.[14] Despite their attributes, some of LSPR sensors still suffer from a lack of sensitivity for biomarker detection in human serum samples. Furthermore, to achieve a considerable response and avoid unexpected nonspecific binding, time-consuming ligand immobilization (covalent coupling) processes are crucially required,[15,16] raising concerns about complicated fabrication procedures and repeatability in clinical disease diagnosis.

Several transformative plasmonic sensors have shown reasonable responses in clinical detection, particularly in studying biomolecular interactions. For example, thermoplasmonic biosensors use plasmonic nanoparticles as photothermal labels, enabling sensitivities up to the attomolar range and the capability of integration with lateral flow assays for rapid POC diagnosis.[17,18] The plasmon ruler is another effective sensing

Dr. J. Nan, Prof. S. Zhu, W. Sun, Dr. Y. Yue, Dr. X. Tang, Prof. J. Zhang, Prof. B. Yang
State Key Laboratory of Supramolecular Structure and Materials
College of Chemistry
Jilin University
Changchun 130021, P. R. China
E-mail: sjzhu@jlu.edu.cn; zjh@jlu.edu.cn
Prof. S. Zhu
Key Laboratory of Organ Regeneration and Transplantation
of the Ministry of Education
The First Hospital of Jilin University
Changchun 130061, P. R. China
Dr. S. Ye
State Key Laboratory of Molecular Engineering of Polymers
Department of Macromolecular Science
Fudan University
Shanghai 200438, P. R. China
Dr. J. Shi, Prof. X. Xu
Department of Clinical Laboratory
China-Japan Union Hospital of Jilin University
Changchun 130033, P. R. China
The ORCID identification number(s) for the author(s) of this article can be found under https://doi.org/10.1002/adma.201905927.

DOI: 10.1002/adma.201905927

platform that records distance changes as a signal by measuring the frequency change of scattered light.[19,20] The dark-field technique is often used to enable the visualization of the scattered Rayleigh light from plasmonic particle dimers.[21–23] However, current plasmonic ruler sensors are also not suitable for POC diagnosis owing to the need for chemical grafting and complex operations.[24–28] Thus, next-generation plasmonic biosensors with improved sensitivity, miniaturization, and facile operation characteristics would be significantly valued.[2]

In this study, to overcome the limitations of current plasmonic biosensors, we demonstrated a proof-of-principle ultrasensitive plasmon ruler platform based on a sandwich-structured Au nanohole array (Au NHA) with analytes placed in the interlayer. Rather than RI changes, we exclusively focused on the thickness change caused by biomolecular absorption, which could be measured precisely by the sandwiched plasmon ruler (SW-PR) over a broad wavelength range from 1400 to 2000 nm. A significant blueshift in the reflectance dip is observed with increasing spacer thickness, and is attributed to the weakened coupling between the Au NHA and the Au layer. In contrast to previous plasmon rulers where half of the charges within the nanoparticles are always positioned away from another, we show that both positive and negative charges concentrate at the bottom of the Au NHA toward the surface of the gold film; thus, the enhanced coupling efficiency greatly improves the response capability of the sensor. To demonstrate the feasibility of the SW-PR platform, we realized the label-free quantification of C-reactive protein (CRP) and procalcitonin (PCT) in patient serum samples without using a prism coupler or chemical immobilization procedure. This next-generation plasmonic biosensor not only provides an unprecedented detection sensitivity for clinical serum samples but also represents a POC platform that is capable of low-cost/large-scale fabrication and facile operation and that features a miniaturized optic fiber detection system.

We initially sought to design the proof-of-principle SW-PR by controlling the key parameters. The general structure of the SW-PR comprised the Au NHA fabricated by colloidal lithography placed on the top, a flat gold film at the bottom, and a detection layer as the sandwiched spacer, as illustrated in **Figure 1**a–d. A polystyrene (PS) interlayer was first employed as an artificial spacer to simulate biomolecules owing to its excellent thickness-tunability (Figure S1 and Table S1, Supporting Information). To construct this Au NHA/spacer/Au system, the Au NHA was first fabricated on a quartz substrate and then placed on a PS-coated Au/quartz substrate via a wet transfer method, as shown in Figure 1c and Figure S2 (Supporting Information). For practical use, the wet transfer method can also be replaced by a rapid HF-free transfer method with improved ease of operation, as shown in Figure S3 of the Supporting Information, where the Au NHA was pretransferred onto a fibrous substrate for long-time storage and can be released by immersing the film in water before use. The transfer time was less than 1 min, followed by a 3 min drying process at room temperature. To comprehensively understand the optical properties of the sandwich system, the transmission spectrum of the Au NHA was first measured, as shown in Figure 1e. The characteristic transmission peaks are predictably attributed to unique Bloch wave SPPs (BW-SPPs) and are described as follows[29,30]

$$\lambda = \frac{P}{\sqrt{\frac{4}{3}\left(i^2 + ij + j^2\right)}} \sqrt{\frac{\varepsilon_{\mathrm{Au}}\varepsilon_{\mathrm{d}}}{\varepsilon_{\mathrm{Au}}+\varepsilon_{\mathrm{d}}}} \tag{1}$$

where P is the period of the nanohole array, $\varepsilon_{\mathrm{Au}}$ and ε_{d} represent the dielectric constants of Au and the surrounding medium, respectively, and i and j are the scattering orders of the array. Thus, the two peaks at 724 and 1026 nm can be assigned as the (1, 0) transmission peaks at the Au/air and Au/substrate interface, respectively, owing to the BW-SPPs.[31] The numbers in brackets denote the values of i and j. In BW-SPP mode, coherent superposition of propagating SPPs results in standing waves on the interface.[8] Notably, surfaces on either side of the nanohole array could support surface plasmon modes. Therefore, the different mediums on the two sides of the surface contribute to two sets of transmission peaks.[32] This unique optical phenomenon was also observed in the form of reflectance dips at 647 and 1552 nm in the reflectance spectrum of the final sandwich system.[30]

We observed that the BW-SPP frequency at the Au/air interface remains almost unchanged, whereas the reflectance dip caused by BW-SPPs at the Au/spacer interface shifts to a longer wavelength, demonstrating that BW-SPPs at the Au/spacer interface couple with the underlying Au film and that the dielectric medium above the Au/air interface remains constant after the transfer procedure.[33,34] Finite-difference time-domain (FDTD) simulations were also consistent with the experimental results, as shown in Figure 1e. Notably, some high-order SPP modes (dips at 781 and 1131 nm) could also be observed and may overlap with other dips under the uncoupling condition.

Based on the efficient signal readout generated by the SW-PR, we next investigated the effect of coupling strength on the reflectance dip shift by finely tuning the thickness of the PS spacer (the spacer thickness was correspondingly adjusted by the concentration of the PS solution used in the spin-coating process). **Figure 2**a shows the geometric parameters of the SW-PR. The inverse-exponential relationship between the wavelength of the reflectance dip and the spacer thickness was observed in an experimental set of six manufactured plasmon rulers (Figure 2b) and was confirmed by FDTD simulations (Figure 2c). This trend is almost the same as that of a standard nanoparticle plasmon ruler based on the near-field coupling effect. Notably, our sandwich system exhibited much higher sensitivity than the standard plasmon ruler.[19]

To reveal the mechanism of ultrahigh sensitivity, FDTD simulations were employed in parallel. The electric field distribution and charge density of the SW-PR with the same experimental parameters were calculated at wavelengths of 652 and 1682 nm, which were considered to correspond to zero-order BW-SPPs at the Au/air and Au/spacer interfaces, respectively (Figure 2d–g). The FDTD data also indicate that, at short wavelengths, the majority of the electric field is distributed on the upper edges of the nanoholes, where the charge density is also concentrated, verifying the experimental observation of propagating SPPs at the Au/air interface and the weak coupling effect between the Au NHA and Au layer. By contrast,

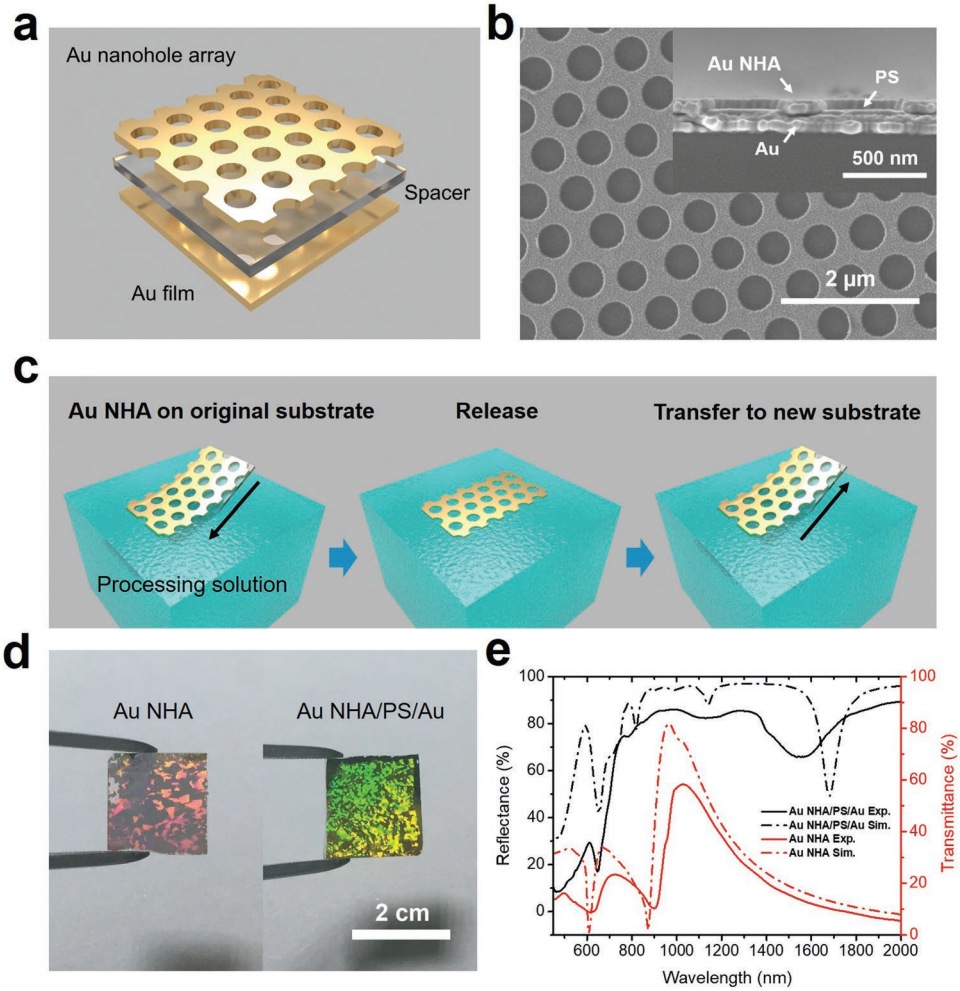

Figure 1. The design of the SW-PR platform featuring distinguishable, electronically fine-tuned reflectance. a) Schematic of the SW-PR platform with a polymer spacer and Au NHA sequentially coated on the Au film. b) Scanning electron micrograph (SEM) of the SW-PR platform. The inset cross-sectional image displays the sandwich structure. The structural subunits are denoted by white arrows. c) Schematic showing the general procedure of the wet transfer method. For instance, when HF solution was used as the processing solution, a temporary quartz substrate was used to transfer the Au NHA to the water surface to remove residual HF before the transfer to the final substrate. d) Physical photographs of the Au NHA film and Au NHA/PS/Au film providing the inherent structural coloration of the nanohole crystals. e) Experimental (solid lines) and FDTD-calculated (dash-dot line) spectra of the Au NHA film and Au NHA/PS/Au film. $P = 695$ nm, $D = 470$ nm, $t = 109.8$ nm, $d = 13.1$ nm.

at long wavelengths, remarkably enhanced electric field localizes in the region of the spacer interlayer, thereby confirming that strong coupling is involved. Importantly, both positive and negative charges are highly concentrated at the bottom of the Au NHA. In the previously reported plasmon ruler derived from nanoparticle dimers, the dipole aligns in parallel, and only half of the charges are attracted by opposite charges within the surrounding nanoparticle.[35,36] In our sandwich system, all highly confined charges are affected by opposite charges on the underlying Au film, and this antisymmetric surface plasmon coupling accordingly possesses comparatively higher coupling efficiency.[37,38] The electric field distribution and charge density of the simple Au NHA calculated by FDTD demonstrated consistent results, as shown in Figure S4 of the Supporting Information. Overall, the concentrated charges caused by propagating SPPs at the two interfaces already existed under uncoupling conditions. Therefore, it could be concluded that the concentrated surface charges caused by BW-SPPs lead to a highly sensitive response to spacer thickness.

Next, we rationally manufactured SW-PR systems with tunable lattice constants, nanohole diameters, and thicknesses of the top Au NHA (Figures S5–S7, Supporting Information), to optimize and boost the sensing performance. We exclusively focused on the property of the reflectance dip at the longer wavelength, which demonstrated the highest sensitivity among all dips. **Figure 3**a–c shows the dip positions of these structures with various spacer thicknesses, indicating that the wavelength of BW-SPPs at the Au/spacer interfaces redshifts with increasing lattice constant or decreasing nanohole size, while the thickness of the nanohole array barely influences the dip position. (standard deviation data are listed in Table S2, Supporting Information) These trends are computationally confirmed by FDTD simulations and are consistent with those of a Au NHA film with the same inherent SPP mode

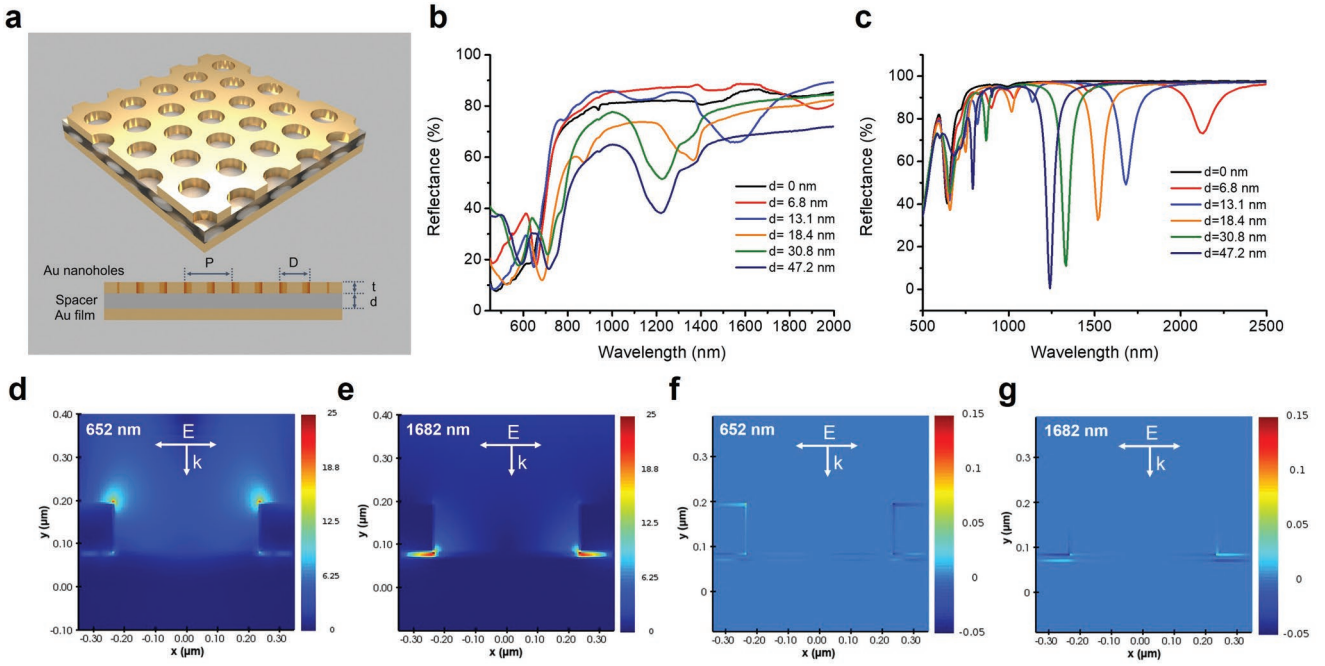

Figure 2. Principle and structurally fine-tuned reflectance of the SW-PR platform. a) Diagram depicting the key parameters for governing the reflectance signal outcomes of the SW-PR platform. b) Measured reflectance spectra of a spacer-thickness-tuned plasmon ruler. c) Calculated reflectance spectra of Au NHA/PS/Au films with experimentally corresponding spacer thicknesses. d,e) Simulated electric field distribution and f,g) simulated charge distribution (cross-sectional view) at excitation wavelengths of 652 and 1682 nm, respectively (P = 695 nm, D = 470 nm, t = 109.8 nm, d = 13.1 nm). The wave vector and polarization direction of the incident plane wave are denoted by white arrows in (d–g).

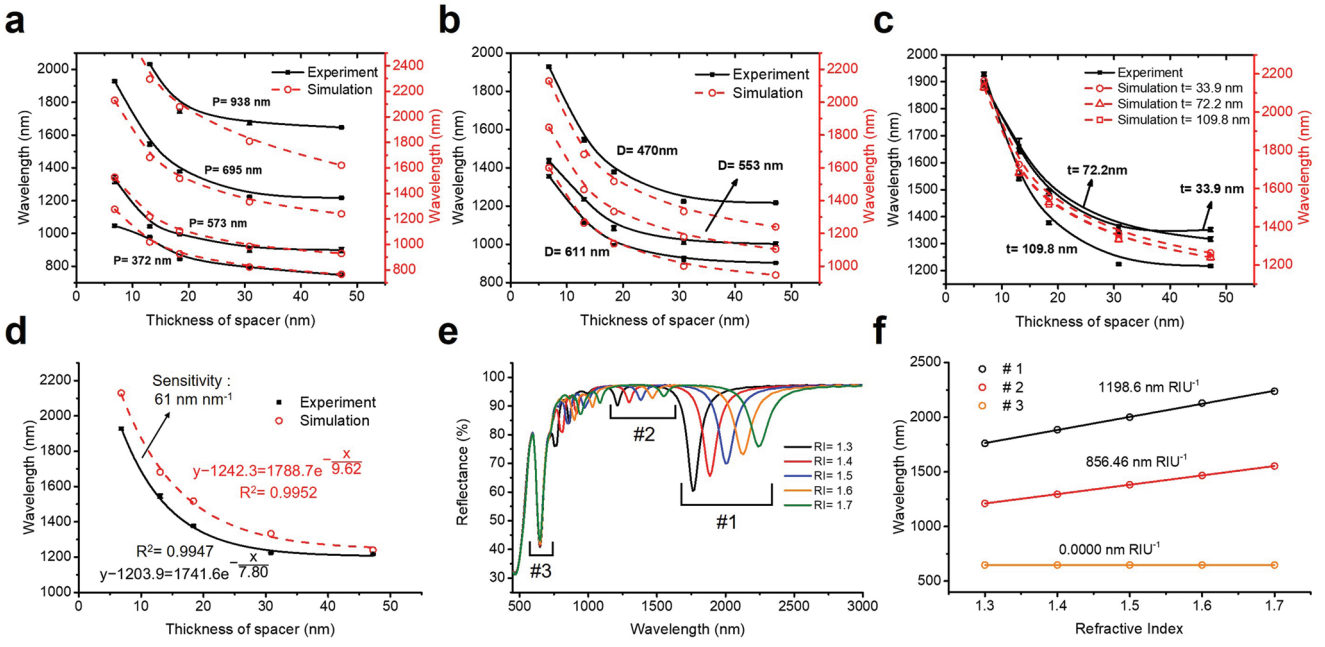

Figure 3. The effect of lattice constant, nanohole diameter, Au NHA thickness, and spacer RI. a–c) Measured and calculated wavelength of the zero-order BW-SPP mode at the Au/spacer interface as a function of spacer thickness with various lattice constants (D/P = 621/938, 470/695, 450/573, and 245/372, t = 109.8 nm), nanohole diameters (P = 695 nm, t = 109.8 nm) and thicknesses of the top Au NHA (P = 695 nm, D = 470 nm). d) Measured and calculated wavelength of the zero-order BW-SPP mode at the Au/spacer interface as a function of spacer thickness with the optimized parameters (P = 695 nm, D = 470 nm, t = 109.8 nm). The exponential decay fit and thickness sensitivity in the thickness range from 6.8 to 13.1 nm are denoted. e) Calculated reflectance spectra of the SW-PR platform with various spacer RIs. Reflectance dips corresponding to the zero-order BW-SPP mode at the Au/spacer interface, a higher-order mode at the Au/spacer interface and the zero-order mode at the Au/air interface are denoted by "#1", "#2", and "#3", respectively. f) Dip positions of "#1", "#2", and "#3" in (e) as a function of spacer RI. For all panels, error bars represent the standard deviation. All experiments were performed in triplicate.

(Figure S8, Supporting Information). In addition, the positions of dips originating from BW-SPPs at the Au/air interface also depend on the parameters mentioned above, which can be suggested by the colors of these samples (Figure S9, Supporting Information). According to Equation (1), it seems that the wavelength of BW-SPPs depends exclusively on the lattice constant. However, the nanohole size actually affects the dip position by changing the propagation constant of SPPs.[39] Finally, the Au NHA/spacer/Au structure with P = 695 nm, D = 470 nm, and t = 109.8 nm was optimally selected for the following sensing events because it had the highest thickness sensitivity in the wavelength range of 1400–2000 nm. The readout sensitivity was calculated to be ≈61 nm nm^{-1} (dip position shifts by ≈61 nm when spacer thickness increases by 1 nm), resulting in an impressive dynamic range of ≈382 nm with thicknesses stretching from 6.8 to 13.1 nm. In addition, the exponential decay fit, which is shown in Figure 3d, is similar to the universal scaling relationship for a plasmonic nanoparticle plasmon ruler,[19,40] suggesting the inherent similarities between the electromagnetic coupling effect in our sandwich system and near-field LSPR coupling.

To precisely quantify the sensitivity, we compared the thickness sensitivity between the SW-PR platform and other reference sensors, including a Au nanowell array (RIS = 681.3 RIU^{-1}), a Ag nanowell array (RIS = 563.1 RIU^{-1}), and Au nanoparticles (RIS = 41.7 RIU^{-1}). The basic optical properties and calculated RIS values of these reference sensors are shown in Figure S10 of the Supporting Information. The comparative results indicated that among the evaluated sensors, our optimal Au NHA/spacer/Au structure with P = 695 nm, D = 470 nm, and t = 109.8 nm exhibited the best performance and was 281-fold more sensitive than the Au nanoparticles, 66-fold more sensitive than the Au nanowell array and 56-fold more sensitive than the Ag nanowell array at thicknesses ranging from 6.8 to 13.1 nm (Figure S11, Supporting Information). Similar results were obtained with FDTD simulations. Different configurations were additionally modeled in our simulations to provide a general rule of performance evaluations. These data show the great thickness sensitivity of the SW-PR platform, which largely exceeds that of current plasmonic sensors.[41,42]

Finally, the effect of the RI of the spacer was investigated by FDTD calculations, as shown in Figure 3e,f. Compared with the thickness factor, the response to the RI of the spacer, which was calculated to be 1198.6 nm RIU^{-1} (zero-order BW-SPP mode) when spacer thickness was set to be 6.8 nm, can be almost neglected. The RI of the surrounding medium does not affect the dip position at the longer wavelength but changes the wavelength of BW-SPPs at the Au/Air interface (Figure S12, Supporting Information), further suggesting that the two SPP modes response to only surrounding medium changes near their respective interfaces. This result also indicates that impurities from the external environment will not affect sensing performance. Overall, remarkably high sensitivity was achieved using the optimized Au NHA/spacer/Au system, making our system suitable for highly sensitive biomolecular sensing.

The developed SW-PR was proven to be highly sensitive to the thickness of an artificial spacer (PS, as investigated above). We next hypothesized that the thickness change caused by the adsorption of clinically relevant biomolecules could be accurately detected by our sensing platform.[43] As illustrated in **Figure 4**a, an additional PS coating of ≈4–6 nm was employed as the adhesive layer to support efficient protein attachment (Figure S13, Supporting Information).[44] Moreover, signals from biomolecular interactions could be shifted into the applicable detection window of the optic fiber detector (Figure S14, Supporting Information). Importantly, the thickness of the additional PS layer needs careful adjustment, as excess thickness failed to direct detection signals into the best sensing wavelength range. A streptavidin (SA)/biotin affinity model where biotin-modified bovine serum albumin (BSA–biotin) was deposited on a PS-coated Au/quartz substrate as a capture protein while the SA pair was diluted in aqueous solution as the detection protein was initially utilized. The wavelength variation curve as a function of the concentration of SA in phosphate buffered saline is shown in Figure 4b. The nanowell sensing platform (RIS = 681.3 and 563.1 nm RIU^{-1} for the Au and Ag nanowell arrays, respectively) reported in the previous work was adopted as a control group under the same detection conditions.[30,45] An extremely large dip shift was observed even at a relatively low concentration (≈13 nm at 0.16×10^{-9} M) using the SW-PR platform, whereas a highly concentrated SA solution caused only a tiny shift (≈3 nm at 160×10^{-9} M) in the nanowell sensing platform control group. There was no obvious apparent color change during the detection (Figure S9, Supporting Information), indicating the relatively low sensitivity of the BW-SPP mode at the Au/Air interface. The thickness of the protein layer was measured by an atomic force microscope (AFM), confirming that the wavelength difference originated, as expected, from the thickness change caused by biomolecular binding/attachment (Figure S15, Supporting Information). The SW-PR platform also exhibited remarkable detection performance when the incubation testing method was applied using a lower concentration of BSA–biotin for protein deposition (Figure 4c). In sharp contrast, Figure 4d revealed that the sensitivity of the Au nanowell sensing platform decreased dramatically when the incubation testing method was employed (relevant original spectra are shown in Figure S16, Supporting Information). These results emphasized the great protein attachment capacity of the PS coating and suggested that the SW-PR platform can detect at least 200 000-fold lower concentration of analytes than the nanowell sensing platform with the same wavelength shift (Calculation Information, Supporting Information).

To further explore the clinical potential of the SW-PR platform, we performed CRP and PCT detection in patient serum samples (**Figure 5**a). A CRP test is the first clinical indicator used to monitor conditions that cause inflammation, including bacterial/fungal infections, inflammatory bowel disease, autoimmune disorder, osteomyelitis, etc.[46] The normal concentration of CRP varies between 0.8 and 3.0 μg mL^{-1} in healthy adults. By contrast, the normal concentration of PCT in the circulation is less than 50 pg mL^{-1}. As a common infectious marker, PCT is related to cardiovascular disease, meningitis, arthritis, and so on.[47] Thus, the accurate detection of these two markers with a broad detection range from pg mL^{-1} to μg mL^{-1} is highly desired in clinical diagnosis. We verified that the SW-PR platform afforded flexible detection ranges and was overqualified for clinical CRP/PCT detection. Figure 5b and

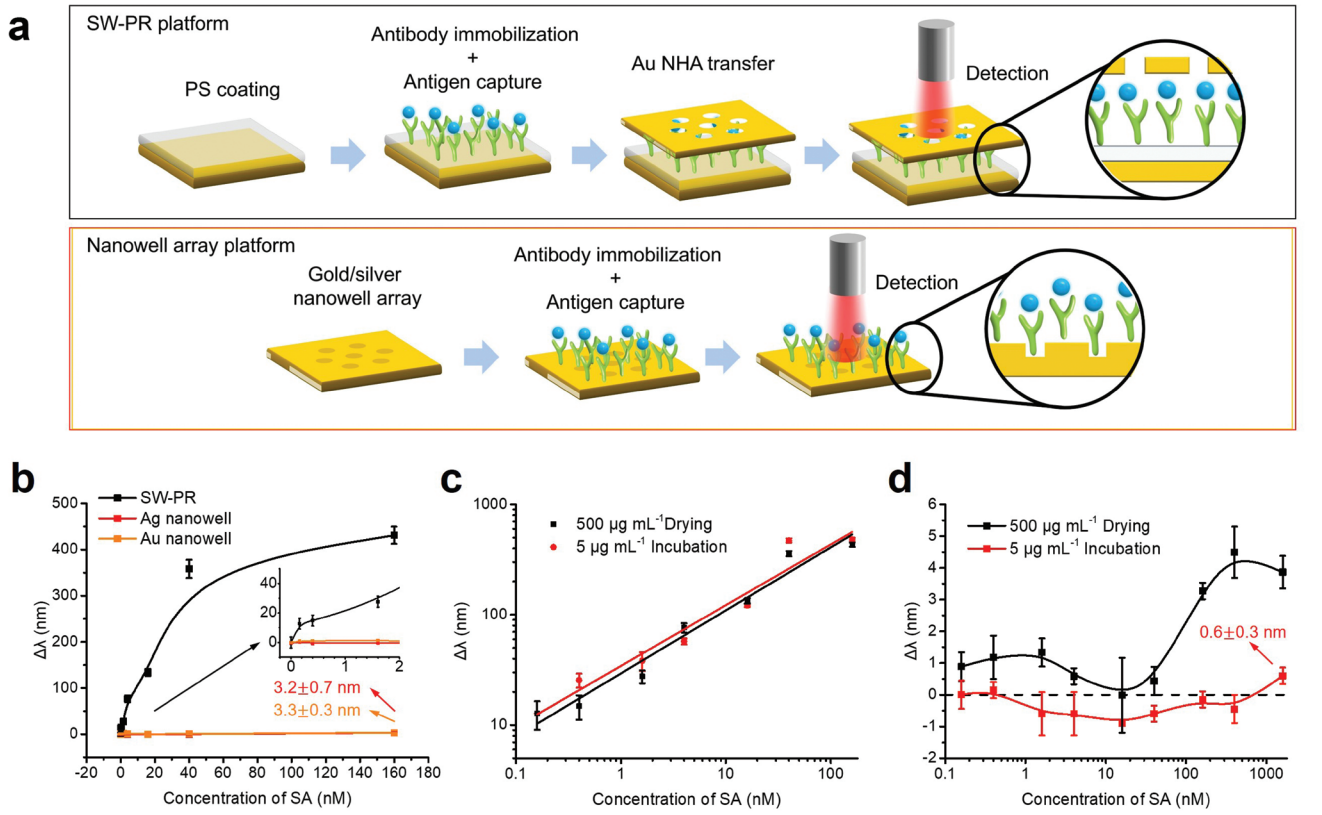

Figure 4. Evaluation of the sensor performance of the SW-PR platform using an SA/biotin affinity model. a) Schematic illustration of the detection procedures of the SW-PR platform and a classic nanowell array platform. The underlying quartz substrate is not shown. The antibody and antigen are replaced with BSA–biotin and SA in the SA/biotin affinity model, respectively. b) Plot of wavelength shift versus SA concentrations using the SW-PR platform and nanowell array platform. The inset shows a zoomed-in view of the graph of the low concentration range. c,d) Wavelength difference as a function of SA concentration using the SW-PR platform (left) and nanowell array platform (right) via two protein loading methods. For all panels, error bars represent the standard deviation. All experiments were performed in triplicate.

Figure S16 (Supporting Information) show the calibration curves and limit of detection (LOD) values for CRP and PCT are 1.81 and 1.24 ng mL^{-1}, respectively. The LOD of the sensing platform was calculated by applying three times the standard deviation to the fitting line of the calibration curves. Using different concentrations of coating solution allowed tunable sensing ranges and broadened the dynamic range, and the lowest LOD (11.9 pg mL^{-1}) was achieved by using a 30 μg mL^{-1} coating solution. In other words, the sensing range could be simply controlled by adjusting the concentration of the coating solution, making our method appropriate for specific disease models where different cut-off values are required. This LOD value was ≈18 times lower than the LOD of an enzyme-linked immunosorbent assay (ELISA), which was measured as 221.7 pg mL^{-1} under the same experimental conditions (Figure 5b), leading to our platform having a broader dynamic range than ELISA. Importantly, the specificity was also investigated, as shown in Figure S17 of the Supporting Information, showing the extremely low cross-interactions with our platform. Furthermore, we collected samples from 38 patients to test our sensing platform (CRP: 11 samples, PCT > 1 ng mL^{-1}: 14 samples, PCT < 5 ng mL^{-1}: 13 samples). PCT serum samples were divided into low and high concentration groups to demonstrate the tunability of the detection range. Figure 5d–i shows that there is no significant difference between the results obtained from our method and the clinical method. Another advantage of the SW-PR platform is its long-term stability (Figure S18, Supporting Information). In contrast to clinical methods, such as ELISA or an immunofluorescence assay, our films could be stored for at least 3 weeks at room temperature without any signal degeneration, because the protein layer was protected by the sandwich structure and because the sensor is insensitive to changes in the surrounding medium, as mentioned above. In conclusion, these data proved the great feasibility of the SW-PR platform and its potential for widespread POC applications. Although not fully achieved in the current report, the strategy of the ultrahigh-sensitivity plasmonic platform will provide an entirely new diagnostic approach for a large number of clinical diseases/events.

There has been an increasing need for rapid label-free diagnosis with high sensitivity in recent years. Among various sensing platforms, nanohole arrays have proven to hold great promise for biomolecular sensing applications due to their unique extraordinary optical transmission.[48–55] This sensing mode could provide a sensitivity of approximately 600 nm per RIU in the visible light range, which is remarkably higher than that provided by plasmonic nanoparticles.[56,57] Therefore, nanohole arrays coupled with microfluidic system are widely used

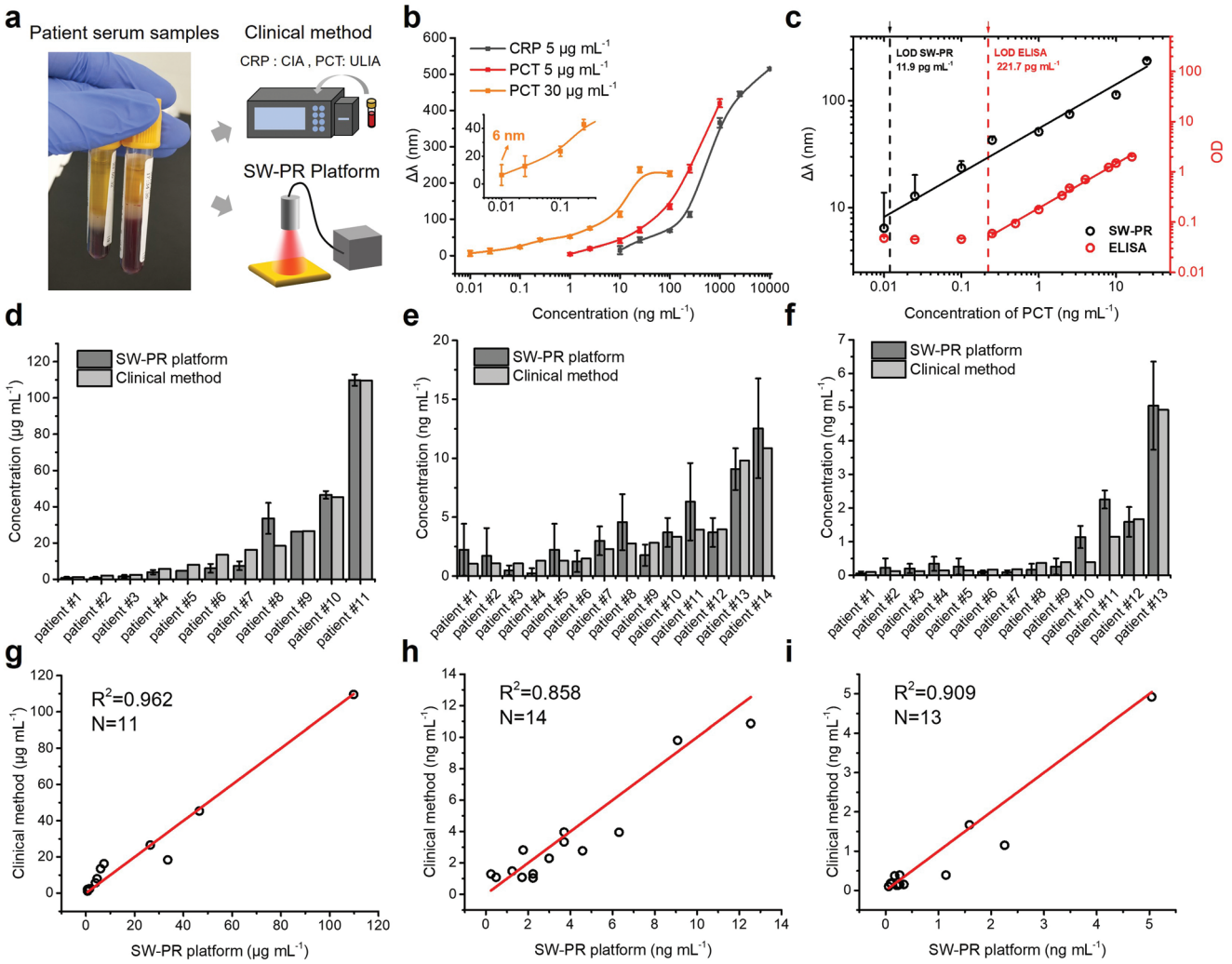

Figure 5. Biomarker detection in clinical patient serum samples. a) Schematic illustration of the PCT and CRP detection procedure. The results obtained from the clinical method were used for comparison. In the clinical method, a chemiluminescence immunoassay (CIA) and an upconversion luminescent immunochromatography assay (ULIA) were used for CRP and PCT detection, respectively. b) Calibration curves for CRP and PCT tested by the SW-PR platform. Two coating concentrations were used for PCT detection (5 and 30 μg mL^{-1}). c) Comparison of calibration curves between the SW-PR platform and ELISA for PCT detection. d–i) Concentrations of biomarkers measured using the SW-PR platform and clinical method and the correlation between data obtained from the two methods. Left: CRP; middle: PCT (>1 ng mL^{-1}); right: PCT (<5 ng mL^{-1}). Red lines in (g–i) represent $y = x$, and R^2 was calculated based on the function $y = x$ rather than the fitting function. For all panels, error bars represent the standard deviation. All samples were tested in triplicate.

in biosensing.[6,8] In our work, the nanohole array was integrated to construct the SW-PR platform. This unique sandwich structure gives rise to an extremely high thickness sensitivity, which is 66 times higher than that of the Au nanowell array. An equivalent RIS of ≈45 000 nm RIU^{-1} is obtained by multiplying this value by the RIS of Au nanowell array. This value is even comparable with the RIS of hyperbolic metamaterials and plasmonic nanorod metamaterials biosensing platforms (30 000 nm RIU^{-1}).[13,58] However, the clinical diagnostic performance of these platforms has not been well explored. As a feasibility demonstration of our platform, we further realized the quantification of clinical samples with a minimum LOD of 11.9 pg mL^{-1} (≈0.8 × 10^{-12} M) without using a chemical immobilization technique or prism coupler. This value is much lower than the typical concentration range of protein biomarkers in clinical samples (≈1 × 10^{-12} to 100 × 10^{-12} M), indicating the potential of this platform for analyzing the vast majority of clinically relevant biomarkers.[59] For this process, the analyte incubation time (0.5 h) is relatively short, and the facile operation results in a total assay time of less than 1.5 h. In sharp contrast, a conventional sandwich immunoassay based on ELISA requires 8 h or longer to perform.[7] In addition, a low-cost colloidal lithography technique and optic fiber detection system, which are considered to be cost-efficient and appropriate for POC diagnosis, were used in the fabrication and detection processes.

Another feature of this sensing platform is that the average thickness of the protein layer, which cannot be measured directly by AFM, can be calculated by substituting the dip wavelength into the scaling relationship of the SW-PR at

0.1 nm resolution. This detection resolution is even comparable with the vertical resolution of AFM. As an illustration, the average thickness of PCT the layer was calculated as shown in Figure S19 of the Supporting Information. This feature will provide a great tool to study the conformational dynamics of biomolecular interactions (such as DNA and proteins), surface chemical reactions, and so on in the dry state. Notably, PCT at a concentration of 10 pg mL^{-1} still causes a relatively large wavelength difference (6 nm) in our sensing platform. Therefore, the sensitivity of this platform could be further improved by using an optical detector with higher resolution, such as a near-infrared spectrophotometer or Fourier infrared spectrometer, for sensing applications that were previously impossible to realize.

In summary, we demonstrated a highly sensitive SW-PR based on a nanohole array for clinical biosensing. Because of the high sensitivity, facile operation, and low-cost instrumentation, this sensing platform is promising for label-free POC diagnosis and would have great implications in the design of next-generation plasmon rulers.

Supporting Information

Supporting Information is available from the Wiley Online Library or from the author.

Acknowledgements

This work was supported by the National Natural Science Foundation of China (Grant Nos. 21774043 and 21975098), the program for JLU Science and Technology Innovative Research Team (2017TD-06), and the opening funds of State Key Laboratory of Applied Optics, Changchun Institute of Optics, Fine Mechanics and Physics, Chinese Academy of Science.

Conflict of Interest

The authors declare no conflict of interest.

Keywords

nanohole arrays, plasmon rulers, plasmonic sensors, point-of-care diagnosis, protein biomarkers

Received: September 10, 2019
Revised: November 14, 2019
Published online:

[1] J. N. Anker, W. P. Hall, O. Lyandres, N. C. Shah, J. Zhao, R. P. Van Duyne, *Nat. Mater.* **2008**, *7*, 442.
[2] J.-F. Masson, *ACS Sens.* **2017**, *2*, 16.
[3] M. Elbahri, M. Abdelaziz, S. Homaeigohar, A. Elsharawy, M. K. Hedayati, C. Röder, M. E. H. Assad, R. Abdelaziz, *Adv. Mater.* **2018**, *30*, 1704442.
[4] T. Endo, K. Kerman, N. Nagatani, H. M. Hiepa, D.-K. Kim, Y. Yonezawa, K. Nakano, E. Tamiya, *Anal. Chem.* **2006**, *78*, 6465.
[5] S. S. Aćimović, H. Šípová-Jungová, G. Emilsson, L. Shao, A. B. Dahlin, M. Käll, T. J. Antosiewicz, *ACS Nano* **2018**, *12*, 9958.
[6] O. Yavas, S. S. Aćimović, J. Garcia-Guirado, J. Berthelot, P. Dobosz, V. Sanz, R. Quidant, *ACS Sens.* **2018**, *3*, 1376.
[7] P. Y. Chen, M. T. Chung, W. McHugh, R. Nidetz, Y. W. Li, J. P. Fu, T. T. Cornell, T. P. Shanley, K. Kurabayashi, *ACS Nano* **2015**, *9*, 4173.
[8] M. E. Stewart, N. H. Mack, V. Malyarchuk, J. A. N. T. Soares, T.-W. Lee, S. K. Gray, R. G. Nuzzo, J. A. Rogers, *Proc. Natl. Acad. Sci. USA* **2006**, *103*, 17143.
[9] T. Y. Xue, W. Y. Liang, Y. W. Li, Y. H. Sun, Y. J. Xiang, Y. P. Zhang, Z. G. Dai, Y. H. Duo, L. M. Wu, K. Qi, B. N. Shivananju, L. J. Zhang, X. Q. Cui, H. Zhang, W. L. Bao, *Nat. Commun.* **2019**, *10*, 28.
[10] B. W. Liu, S. Chen, J. C. Zhang, X. Yao, J. H. Zhong, H. X. Lin, T. X. Huang, Z. L. Yang, J. F. Zhu, S. Liu, C. Lienau, L. Wang, B. Ren, *Adv. Mater.* **2018**, *30*, 1706031.
[11] F. Yesilkoy, R. A. Terborg, J. Pello, A. A. Belushkin, Y. Jahani, V. Pruneri, H. Altug, *Light: Sci. Appl.* **2018**, *7*, 17152.
[12] M. E. Stewart, C. R. Anderton, L. B. Thompson, J. Maria, S. K. Gray, J. A. Rogers, R. G. Nuzzo, *Chem. Rev.* **2008**, *108*, 494.
[13] K. V. Sreekanth, Y. Alapan, M. ElKabbash, E. Ilker, M. Hinczewski, U. A. Gurkan, A. De Luca, G. Strangi, *Nat. Mater.* **2016**, *15*, 621.
[14] A. Csáki, O. Stranik, W. Fritzsche, *Expert Rev. Mol. Diagn.* **2018**, *18*, 279.
[15] P. Singh, *Surface Plasmon Resonance*, Nova Science Pub. Inc., New York, USA **2014**.
[16] F. Inci, O. Tokel, S. Q. Wang, U. A. Gurkan, S. Tasoglu, D. R. Kuritzkes, U. Demirci, *ACS Nano* **2013**, *7*, 4733.
[17] E. Polo, P. Del Pino, B. Pelaz, V. Grazua, J. M. de la Fuente, *Chem. Commun.* **2013**, *49*, 3676.
[18] Z. P. Qin, W. C. W. Chan, D. R. Boulware, T. Akkin, E. K. Butler, J. C. Bischof, *Angew. Chem., Int. Ed.* **2012**, *51*, 4358.
[19] L. X. Wu, B. M. Reinhard, *Chem. Soc. Rev.* **2014**, *43*, 3884.
[20] L. L. Yang, H. Y. Wang, B. Yan, B. M. Reinhard, *J. Phys. Chem. C* **2010**, *114*, 4901.
[21] L. Lermusiaux, V. Maillard, S. Bidault, *ACS Nano* **2015**, *9*, 978.
[22] L. Lermusiaux, S. Bidault, *Langmuir* **2018**, *34*, 14946.
[23] V. Pini, P. M. Kosaka, J. J. Ruz, O. Malvar, M. Encinar, J. Tamayo, M. Calleja, *Sci. Rep.* **2016**, *6*, 22836.
[24] C. Sönnichsen, B. M. Reinhard, J. Liphardt, A. P. Alivisatos, *Nat. Biotechnol.* **2005**, *23*, 741.
[25] J. I. L. Chen, C. Yeechi, D. S. Ginger, *J. Am. Chem. Soc.* **2010**, *132*, 9600.
[26] G. X. Rong, H. Y. Wang, B. M. Reinhard, *Nano Lett.* **2010**, *10*, 230.
[27] S. E. Lee, Q. Chen, R. Bhat, S. Petkiewicz, J. M. Smith, V. E. Ferry, A. L. Correia, A. P. Alivisatos, M. J. Bissell, *Nano Lett.* **2015**, *15*, 4564.
[28] J. I. L. Chen, H. Durkee, B. Traxler, D. S. Ginger, *Small* **2011**, *7*, 1993.
[29] S.-H. Chang, S. K. Gray, G. C. Schatz, *Opt. Express* **2005**, *13*, 3150.
[30] S. S. Ye, X. M. Zhang, L. X. Chang, T. Q. Wang, Z. B. Li, J. H. Zhang, B. Yang, *Adv. Opt. Mater.* **2014**, *2*, 779.
[31] X. M. Zhang, Z. B. Li, S. S. Ye, S. Wu, J. H. Zhang, L. Y. Cui, A. R. Li, T. Q. Wang, S. Z. Li, B. Yang, *J. Mater. Chem.* **2012**, *22*, 8903.
[32] C. Genet, T. W. Ebbesen, *Nature* **2007**, *445*, 39.
[33] C. Stelling, S. Fossati, J. Dostalek, M. Retsch, *Nanoscale* **2018**, *10*, 17983.
[34] G. Behera, S. A. Ramakrishna, *J. Phys. D: Appl. Phys.* **2016**, *49*, 075103.
[35] I. Romero, J. Aizpurua, G. W. Bryant, F. J. G. De Abajo, *Opt. Express* **2006**, *14*, 9988.
[36] W. Rechberger, A. Hohenau, A. Leitner, J. R. Krenn, B. Lamprecht, F. R. Aussenegg, *Opt. Commun.* **2003**, *220*, 137.
[37] C. G. Hu, Z. Y. Zhao, X. N. Chen, X. G. Luo, *Opt. Express* **2009**, *17*, 11039.
[38] G. Dayal, S. A. Ramakrishna, *Opt. Express* **2012**, *20*, 17503.

[39] R. Gordon, A. G. Brolo, A. McKinnon, A. Rajora, B. Leathem, K. L. Kavanagh, *Phys. Rev. Lett.* **2004**, *92*, 037401.
[40] S. Lerch, B. M. Reinhard, *Adv. Mater.* **2016**, *28*, 2030.
[41] S. Tadepalli1, Z. F. Kuang, Q. S. Jiang, K.-K. Liu, M. A. Fisher, J. J. Morrissey, E. D. Kharasch, J. M. Slocik, R. R. Naik, S. Singamaneni, *Sci. Rep.* **2015**, *5*, 16206.
[42] F. Mazzotta, T. W. Johnson, A. B. Dahlin, J. Shaver, S.-H. Oh, F. Höök, *ACS Photonics* **2015**, *2*, 256.
[43] M. Holgado, F. J. Sanza, A. López, A. Laví, R. Casquel, M. F. Laguna, *Sensors* **2014**, *14*, 3675.
[44] M. Rabe, D. Verdes, S. Seeger, *Adv. Colloid Interface Sci.* **2011**, *162*, 87.
[45] P. H. Xue, S. S. Ye, H. Y. Su, S. L. Wang, J. J. Nan, X. C. Chen, W. D. Ruan, J. H. Zhang, Z. C. Cui, B. Yang, *Nanoscale* **2017**, *9*, 6724.
[46] K. H. Allin, B. G. Nordestgaard, *Crit. Rev. Clin. Lab. Sci.* **2011**, *48*, 155.
[47] P. Schuetz, W. Albrich, B. Mueller, *BMC Med.* **2011**, *9*, 107.
[48] R. Gordon, D. Sinton, K. L. Kavanagh, A. G. Brolo, *Acc. Chem. Res.* **2008**, *41*, 1049.
[49] C. Lertvachirapaiboon, A. Baba, S. Ekgasit, K. Shinbo, K. Kato, F. Kaneko, *Biosens. Bioelectron.* **2018**, *99*, 399.
[50] T.-Y. Chang, M. Huang, A. A. Yanik, H.-Y. Tsai, P. Shi, S. Aksu, M. F. Yanik, H. Altug, *Lab Chip* **2011**, *11*, 3596.
[51] S. H. Lee, N. C. Lindquist, N. J. Wittenberg, L. R. Jordan, S.-H. Oh, *Lab Chip* **2012**, *12*, 3882.
[52] H. Im, H. L. Shao, Y. I. Park, V. M. Peterson, C. M. Castro, R. Weissleder, H. Lee, *Nat. Biotechnol.* **2014**, *32*, 490.
[53] J. Henzie, M. H. Lee, T. W. Odom, *Nat. Nanotechnol.* **2007**, *2*, 549.
[54] A. Belushkin, F. Yesilkoy, H. Altug, *ACS Nano* **2018**, *12*, 4453.
[55] Y. J. Ke, S. S. Ye, P. Hu, H. Jiang, S. C. Wang, B. Yang, J. H. Zhang, Y. Long, *Mater. Horiz.* **2019**, *6*, 1380.
[56] A.-P. Blanchard-Dionne, M. Meunier, *Adv. Opt. Photonics* **2017***9*, 891.
[57] X. Y. Liu, W. D. Liu, L. P. Fang, S. S. Ye, H. Z. Shen, B. Yang. *Nano Res.* **2017**, *10*, 908.
[58] A. V. Kabashin, P. Evans, S. Pastkovsky, W. Hendren, G. A. Wurtz, R. Atkinson, R. Pollard, V. A. Podolskiy, A. V. Zayats, *Nat. Mater.* **2009**, *8*, 867.
[59] J. D. Spitzberg, A. Zrehen, X. F. van Kooten, A. Meller, *Adv. Mater.* **2019**, *31*, 1900422.